AGU PUBLICATIONS

JGR

Journal of Geophysical Research: Atmospheres

RESEARCH ARTICLE
10.1002/2014JD022792

Key Points:
- Performance of ellipsoids in modeling volcano ash optical properties is studied
- Volcano ash measurements, e.g., Eyjafjallajokull, are used as references
- Ellipsoids work well in modelling the scattering matrix of volcanic ash

Correspondence to:
S. Merikallio,
Sini.Merikallio@fmi.fi

Citation:
Merikallio, S., O. Muñoz, A.-M. Sundström, T. H. Virtanen, M. Horttanainen, G. de Leeuw, and T. Nousiainen (2015), Optical modeling of volcanic ash particles using ellipsoids, *J. Geophys. Res. Atmos.*, *120*, 4102–4116, doi:10.1002/2014JD022792.

Received 31 OCT 2014
Accepted 25 MAR 2015
Accepted article online 28 MAR 2015
Published online 4 May 2015

Optical modeling of volcanic ash particles using ellipsoids

Sini Merikallio[1], Olga Muñoz[2], Anu-Maija Sundström[3], Timo H. Virtanen[1], Matti Horttanainen[1], Gerrit de Leeuw[1,3], and Timo Nousiainen[1]

[1]Finnish Meteorological Institute, Helsinki, Finland, [2]Instituto de Astrofísica de Andalucía, CSIC, Spain, [3]Department of Physics, University of Helsinki, Helsinki, Finland

Abstract The single-scattering properties of volcanic ash particles are modeled here by using ellipsoidal shapes. Ellipsoids are expected to improve the accuracy of the retrieval of aerosol properties using remote sensing techniques, which are currently often based on oversimplified assumptions of spherical ash particles. Measurements of the single-scattering optical properties of ash particles from several volcanoes across the globe, including previously unpublished measurements from the Eyjafjallajökull and Puyehue volcanoes, are used to assess the performance of the ellipsoidal particle models. These comparisons between the measurements and the ellipsoidal particle model include consideration of the whole scattering matrix, as well as sensitivity studies on the point of view of the Advanced Along Track Scanning Radiometer (AATSR) instrument. AATSR, which flew on the ENVISAT satellite, offers two viewing directions but no information on polarization, so usually only the phase function is relevant for interpreting its measurements. As expected, ensembles of ellipsoids are able to reproduce the observed scattering matrix more faithfully than spheres. Performance of ellipsoid ensembles depends on the distribution of particle shapes, which we tried to optimize. No single specific shape distribution could be found that would perform superiorly in all situations, but all of the best-fit ellipsoidal distributions, as well as the additionally tested equiprobable distribution, improved greatly over the performance of spheres. We conclude that an equiprobable shape distribution of ellipsoidal model particles is a relatively good, yet enticingly simple, approach for modeling volcanic ash single-scattering optical properties.

1. Introduction

Volcanic eruptions, in particular the explosive types, may generate vast amounts of volcanic ash, which is then dispersed in the atmosphere. This ash can be transported over large distances, depending on the plume height, meteorological conditions, and ash particle size. By absorbing, emitting, and scattering electromagnetic radiation, processes all described by so-called optical properties, these particles may induce considerable environmental impacts [*Bertrand et al.*, 1999; *Mather et al.*, 2013; *Bignami et al.*, 2013], potentially even blurring the effects of anthropogenic climate change for a while [*Hyde and Crowley*, 2000; *Bertrand et al.*, 2002]. In addition to radiative effects, volcanic products can also change atmospheric chemistry considerably [*McGee et al.*, 1994] and induce health hazards, especially respiratory problems [*Baxter et al.*, 1982; *Horwell and Baxter*, 2006; *Gudmundsson*, 2011]. These health effects depend on particle properties, namely, size, composition, and surface characteristics [*Horwell and Baxter*, 2006], all of which can vary between sources and even as a function of the ash plume age due to chemical and physical processes taking place within the newly erupted matter [*Mather et al.*, 2013]. These same traits also affect the way ash particles scatter and absorb light, namely, refractive index of the scattering material, scattering and absorption cross sections, and scattering phase function. Also, we are not able to forecast volcanic eruptions well [*Sparks*, 2003], and while in the atmosphere, ash particles may interfere with aviation activities causing considerable economic losses [*Casadevall*, 1994; *Guffanti et al.*, 2010; *Prata et al.*, 2014]. For these reasons the remote detection and global monitoring of ash clouds is of great interest.

Volcanic ash particles are irregularly shaped and can be substantially porous [*Heiken*, 1974; *Riley et al.*, 2003]. Modeling optical properties of such particles accurately can be extremely challenging, while being crucially important for reliable remote sensing observations of atmospheric ash. Inadequate optical models may lead, for example, to ash plumes misidentified as other types of particles by the retrieval algorithm, as happened with the Multi-angle Imaging SpectroRadiometer (MISR) satellite instrument during Eyjafjallajökull eruption [*Kahn and Limbacher*, 2012]. Also, present satellite retrieval algorithms may be unable to identify large ash

particles [*Stevenson et al.*, 2015; *Kylling et al.*, 2014]. As of yet, optical modeling based on morphologically faithful model particles cannot cover the whole range of optically important ash particles present in the atmosphere [*Kahnert et al.*, 2014]. It is thus highly desirable to establish whether simpler model particles could be used to mimic the volcanic ash optical properties adequately, which is why we study here whether simple yet flexible ellipsoidal model particles could be used as a proxy for ash in remote sensing retrievals. This is done by comparing model simulations based on ellipsoids with laboratory-measured scattering matrices for real volcanic ash samples. We also investigate the performance of the ellipsoid model for use with the Advanced Along Track Scanning Radiometer (AATSR) retrievals, taking into account the specific angle span visible to the instrument and focusing on the phase function.

The shape of an ellipsoid greatly affects the way it scatters light. Scattering by an ensemble of ellipsoids is thus dependent on the relative proportions of different shapes, i.e., the shape distribution of the ensemble. We aim at deriving a generic shape distribution of ellipsoidal model particles that would closely mimic scattering by volcanic ash particles and could thus be used as a first guess in modeling light scattering by ash of any volcano.

Because volcanic ash particles are neither ellipsoidal nor homogenous, it is far from obvious that such particles could mimic the optical properties of ash particles realistically. Therefore, we not only test the performance of ellipsoids in mimicking the optical properties of volcanic ash particles but also analyze the shape distributions that provide the best performance for different laboratory data. The latter is to establish whether a generic shape distribution could be proposed for the optical modeling of ash particles. It is noted that if the shape distribution can be fixed, then the optical properties predicted by ellipsoids depend only on the refractive index and size parameter, exactly as is the case for Mie spheres, making the application of ellipsoids simpler. The fact that ellipsoids have been previously shown to mimic well the optical properties of mineral dust particles present in the terrestrial and Martian atmosphere [*Bi et al.*, 2009; *Merikallio et al.*, 2013], which are also nonellipsoidal and inhomogeneous particles, suggests that ellipsoids might nevertheless perform adequately also for mimicking ash optical properties.

Figure 1 shows the locations of all volcanoes from which the ash samples studied in this paper were collected. A number of different samples collected from world-wide locations are used to assure that the findings are generic. Eyjafjallajökull and Puyehue ash scattering measurements are presented in this paper, but others have been published before by *Volten et al.* [2001] and *Muñoz et al.* [2004]. The locations are scattered widely over the globe, emphasizing the global relevance of volcanic eruptions. Sampled volcanoes are situated in subduction zones except Eyjafjallajökull, which lies in a rift zone. All of these volcanoes can produce ash clouds as a result of the explosive nature of their eruptions. Partly this is a result of their mineral compositions, particularly the relatively high amount of SiO_2 in magma and partly of interaction with water, as is the case with Eyjafjallajökull [*Gudmundsson et al.*, 2008]. Composition and optical characteristics of the samples can be expected to vary. Thus, if a model is found that works adequately in modeling all of the samples, it can reasonably be expected to perform adequately also on modeling future eruptions, regardless of their location.

2. Laboratory Measurements

Measurements are needed as a reference to which the modeling approach, i.e., using ellipsoidal particles to model optical properties of the volcanic ash particles (as described in Section 3), can be compared to assess the validity of this approach. In this section we present and discuss new light scattering measurements (scattering matrices) for Eyjafjallajökull and Puyehue volcanic ash samples. The measurements have been performed at the IAA CODULAB in Granada. The measurements corresponding to the other volcanic ash samples considered in this paper, namely, Pinatubo, Lokon, Mount St. Helens, Spurr Ashton, and Redoubt volcanoes, were performed at the Amsterdam Light scattering setup [*Hovenier*, 2000] and have previously been published by *Volten et al.* [2001] and *Muñoz et al.* [2004].

2.1. Volcanic Ash Samples

The Puyehue ash sample originates from the June 2011 eruption of the Puyehue-Cordón Caulle complex. The sample was collected from the surface deposit at a distance of around 150 km from the epicenter of the eruption in the Comallo region. A rhyolitic obsidian composition could be assumed for the Puyehue ash [*Newman et al.*, 2012] with a complex refractive index m of $1.48 + 0.00027i$ [*Pollack et al.*, 1974].

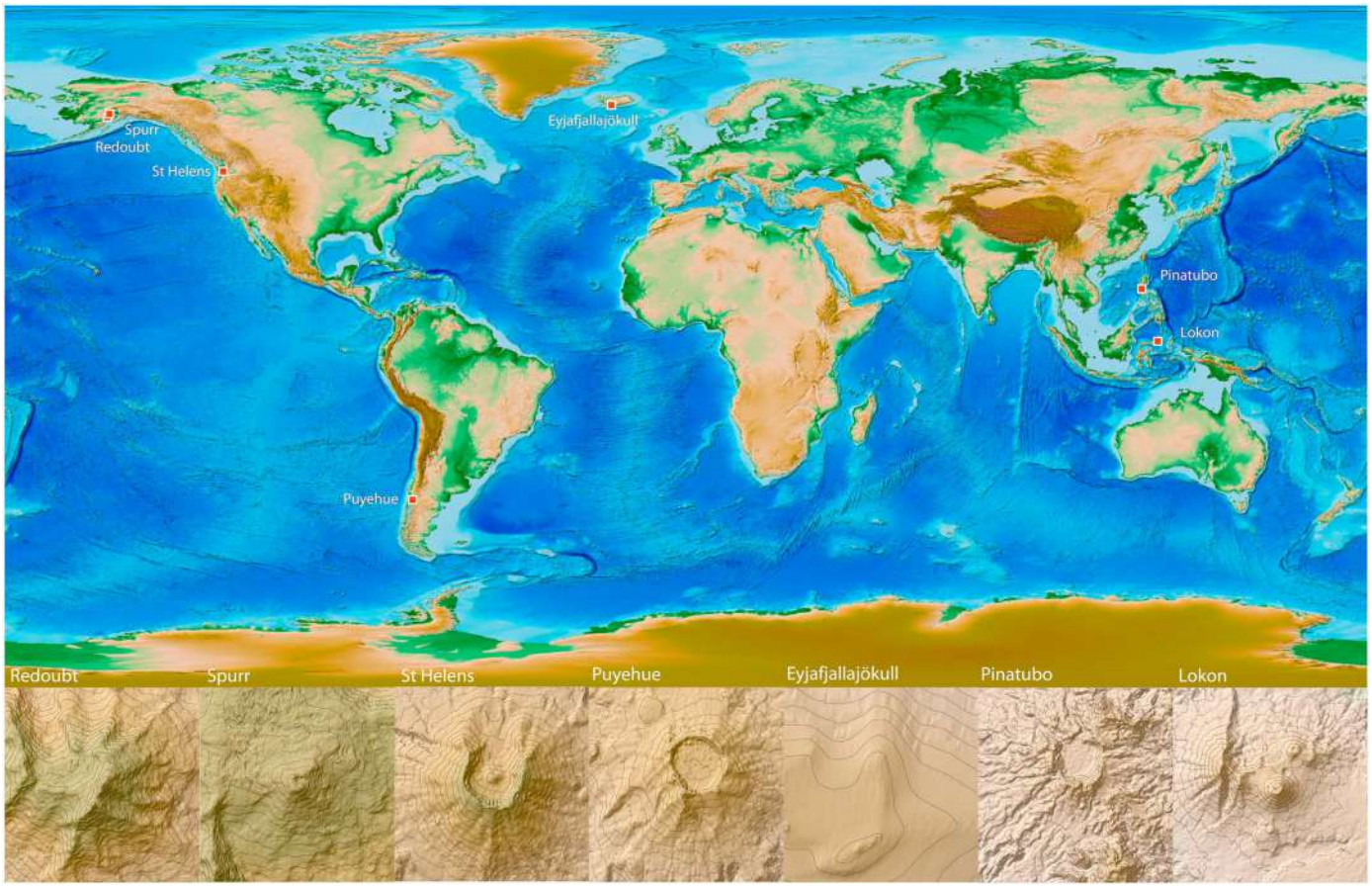

Figure 1. Map showing the locations of the volcanoes used here for model validation. Also shown are close-ups of each volcano within a 10×10 km^2 box showing the height contours with 100 m of vertical difference between the lines.

The Eyjafjallajökull ash sample was collected from the surface deposit right after the April 2010 eruption at 5 km from the source. Estimates of the real part of the refractive index in the spectral region at which we have performed our light scattering measurements (647.0 nm) range from 1.43 [*Newman et al.*, 2012] to 1.49 for the fine grain mode (diameter 0.1 – 0.6 μm) and from 1.52 [*Newman et al.*, 2012] to 1.59 [*Schumann et al.*, 2011] for the coarse mode (diameter of 0.6 – 35 μm). The imaginary part varies from non-absorbing particles [*Schumann et al.*, 2011; *Newman et al.*, 2012] to 0.0012 [*Rocha-Lima et al.*, 2014] for the fine mode and 0.0015 [*Newman et al.*, 2012; *Rocha-Lima et al.*, 2014] to 0.004 [*Schumann et al.*, 2011] for the coarse mode. In the modeling part of this work, however, we have decided to use a different refractive index value of $1.55 + 0.001i$ for both Puyehue and Eyjafjallajökull samples because this produced better fits, as explained in section 3.

In Figure 2 we present Scanning Electron Microscope (SEM) images of the samples discussed in this paper, including those of the Eyjafjallajökull and Puyehue ash particles. These particles show the characteristic shapes of volcanic ash particles [*Maria and Carey*, 2002; *Riley et al.*, 2003]. In particular, they contain vesicular (interspersed by cavities) particles and crystals with sharp edges. It is noted that these SEM pictures are not representative for the particle size distributions of the samples; the latter were obtained as explained in the next subsection.

2.2. Size Distribution Measurements

The volume distribution of the Eyjafjallajökull and Puyehue samples were measured with a Mastersizer2000 from Malvern instruments; these volume distributions were then converted to number size distributions. The Mastersizer2000 measures the phase function of the sample at a wavelength of 632.8 nm over a certain range of scattering angles with special attention to the forward scattering peak. The measured phase function is used to retrieve the volume distribution by matching the angular patterns to those simulated by the instrument software. In the simulations, either Lorenz-Mie or Fraunhofer theory is applied. Both options make an

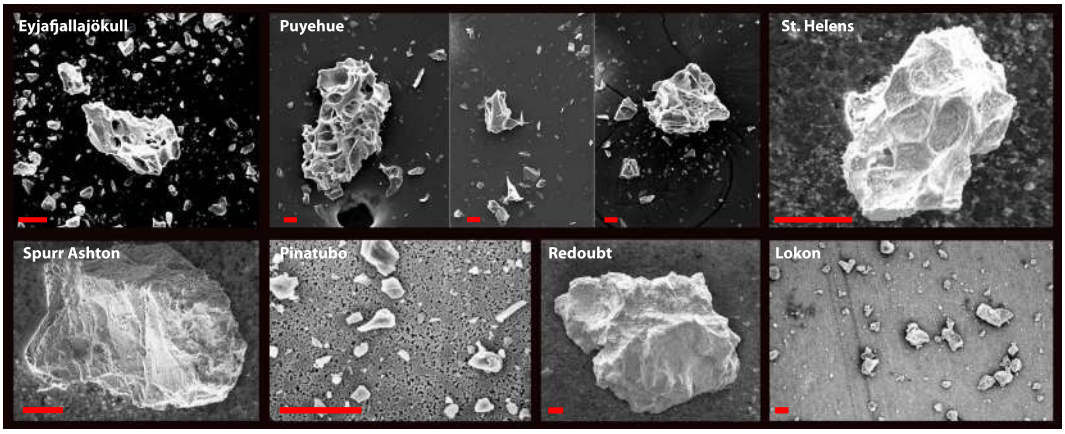

Figure 2. Collage of SEM-pictures for each of the volcanic ash samples discussed in this paper. The red bars equal 20 μm in all cases.

inherent assumption that the measured particles are spherical. Moreover, unlike the Lorenz-Mie method, the Fraunhofer method is an approximation which is not suitable for particles with sizes similar to or smaller than the instrument's wavelength. As our volcanic ash samples contain particles with sizes in the submicron range, it must be assumed that the Lorenz-Mie option might provide more accurate size distribution measurements in the mentioned size range. In general, as is shown in Table 1, the retrieved effective radii from the Lorenz-Mie theory are larger than those obtained with the Fraunhofer theory. As expected, results of both sizing methods tend to converge as the particles become larger. The retrieved size distributions for Puyehue and Eyjafjallajökull samples are shown in Figure 3.

The size distributions of the Pinatubo, Lokon, Mount St. Helens, Redoubt A, and Mount Spurr samples were measured in Amsterdam by using a Fritsch laser particle sizer [*Konert and Vandenberghe*, 1997] which employs the Fraunhofer diffraction theory for spheres. This instrument measures a projected surface-area distribution, which is then converted to number size distribution. As the Fritsch laser sizer does not have the option to use the exact Lorenz-Mie theory, these samples were measured again, about 10 years later, with the Mastersizer2000 in Granada, Spain. When using the Fraunhofer mode, values for the effective radius, r_{eff}, and effective variance, v_{eff} (as defined in [*Hansen and Travis*, 1974]), similar to those obtained in Amsterdam, were only obtained for the St. Helens sample, for which $r_{\mathrm{eff}} = 4.1$ μm and $v_{\mathrm{eff}} = 9.5$ were measured in Amsterdam and $r_{\mathrm{eff}} = 4.3$ μm and $v_{\mathrm{eff}} = 8.1$ 10 years later in Granada. This finding provides confidence in that the size distribution retrieved from the Mount St. Helens sample has not significantly changed in time (due to, e.g., atmospheric humidity). Therefore, we also retrieved the size distribution for it again in Granada by using the Lorenz-Mie mode. For the other samples later size distribution retrievals are either lacking or deliver over 0.4 μm larger values for the effective radius, sowing doubt on the representativeness of using the newer measurements in connection with the scattering matrices measured in Amsterdam. For these reasons, we consider the samples in two groups: one for which we have trustworthy Lorenz-Mie measurements available (Mount St. Helens, Puyehue, and Eyjafjallajökull) and the other for which we used the originally measured Fraunhofer

Table 1. Properties of Measured Volcanic Ash Particles

	Mie		Fraunhofer		Refractive Index		Wavelength
Sample	r_{eff} [μm]	v_{eff}	r_{eff} [μm]	v_{eff}	m_{r},	m_{i} (estimated)	λ[nm]
Eyjafjallajökull	7.8	2.9	4.0	5.9	[1.43–1.59]	+ i[0 – 0.004]	647.0
Lokon			7.0	2.5	[1.5–1.6]	+ i[0.001 – 0.00001]	441.6 & 632.8
Pinatubo	8.0	5.1	2.9	12.4	[1.5–1.6]	+ i[0.001 – 0.00001]	441.6 & 632.8
Puyehue	8.6	2.2	5.0	4.4	1.48	+ i0.00027	647.0
Redoubt A			4.1	9.7	[1.48–1.56]	+ i0.0018	632.8
Spurr Ashton	5.2	3.4	2.6	4.9	[1.48–1.56]	+ i[0.0018 – 0.02]	632.8
St. Helens	8.9	4.0	4.1	9.5	[1.48–1.56]	+ i0.0018	632.8

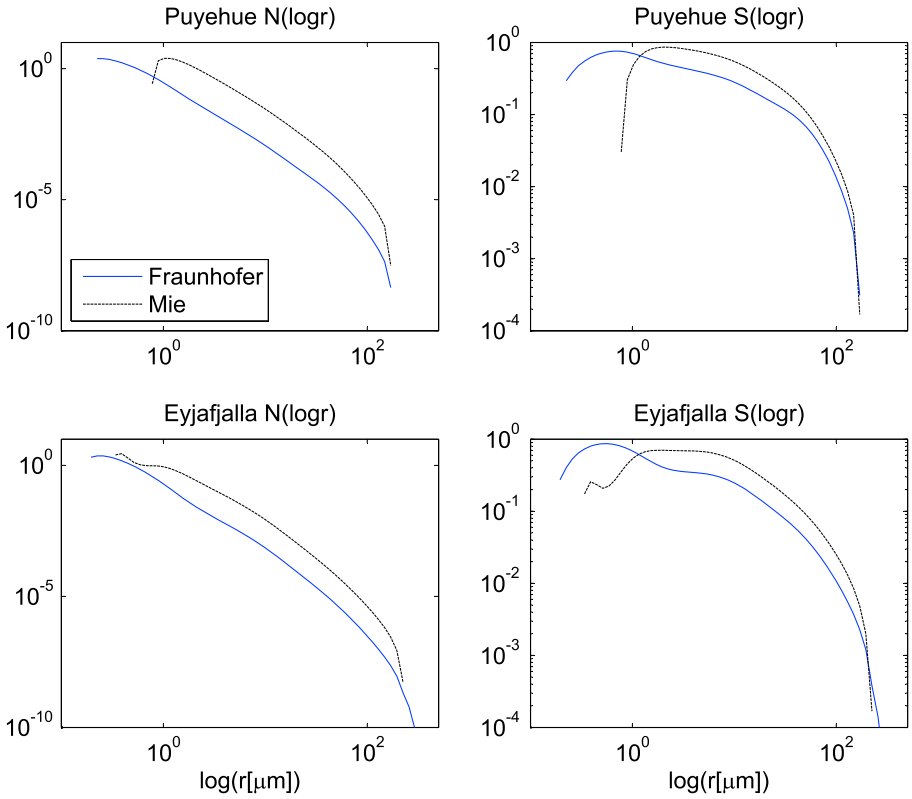

Figure 3. Measured size distributions S(logr) and N(logr), for projected surface area and particle number concentrations, respectively, retrieved from Puyehue and Eyjafjallajökull samples by using both Fraunhofer and Mie theories.

size-distribution (Pinatubo, Lokon, Redoubt A, and Mount Spurr). The calculated effective radii and variances, estimated refractive indices, and the wavelengths for which the scattering matrices have been measured are summarized in Table 1. Tables for normalized number, projected-surface-area, and volume size distributions for the volcanic ash samples are available in the Amsterdam-Granada Light Scattering Database [*Muñoz et al.*, 2010].

2.3. Scattering Measurements

The scattering matrices of the Eyjafjallajökull and Puyehue samples were measured at the IAA COsmic DUst LABoratory (CODULAB) located at the Instituto de Astrofísica de Andalucía, Granada, Spain. Briefly, as a light source we use an Argon-Krypton laser tuned at 647 nm. The laser beam passes through a polarizer and an electro-optic modulator. The modulated light is subsequently scattered by an ensemble of randomly oriented ash particles located in a jet stream produced by an aerosol generator. The scattered light passes through a quarter-wave plate and an analyzer (both optional) and is detected by a photomultiplier tube which moves along a ring. In this way scattering angles from 3° to 177° are covered in the measurements. Another photomultiplier tube located at a fixed position is used to detect and correct for fluctuations in the signal. We employ polarization modulation in combination with lock-in detection to obtain the entire four-by-four scattering matrix. Special tests have been performed to ensure that our experiment is performed under the single-scattering regime [*Muñoz et al.*, 2011]. We also check that the measurements fulfill the Cloude coherency matrix test given in [*Hovenier et al.*, 1986] within the experimental errors at all measured scattering angles. For a detailed description of the experimental apparatus, calibration process, and data acquisition, we refer to [*Muñoz et al.*, 2010].

The measured scattering matrices for the Eyjafjallajökull and Puyehue samples at 647 nm are presented in Figure 4. The measured scattering matrix **F** is related to the phase matrix **P** by $\mathbf{F} = a\mathbf{P}$, where a is some unknown normalization factor. All matrix elements (except F_{11} itself) are normalized to F_{11}; that is, we consider F_{ij}/F_{11}, with ij = 12, 22, 33, 34, or 44. Due to the unknown a, values of $F_{11}(\theta)$ are re-normalized so that F_{11} equals unity at the scattering angle $\theta = 30°$, thus making different samples comparable. The measurements are presented together with the average scattering matrix for volcanic ash obtained from the measured

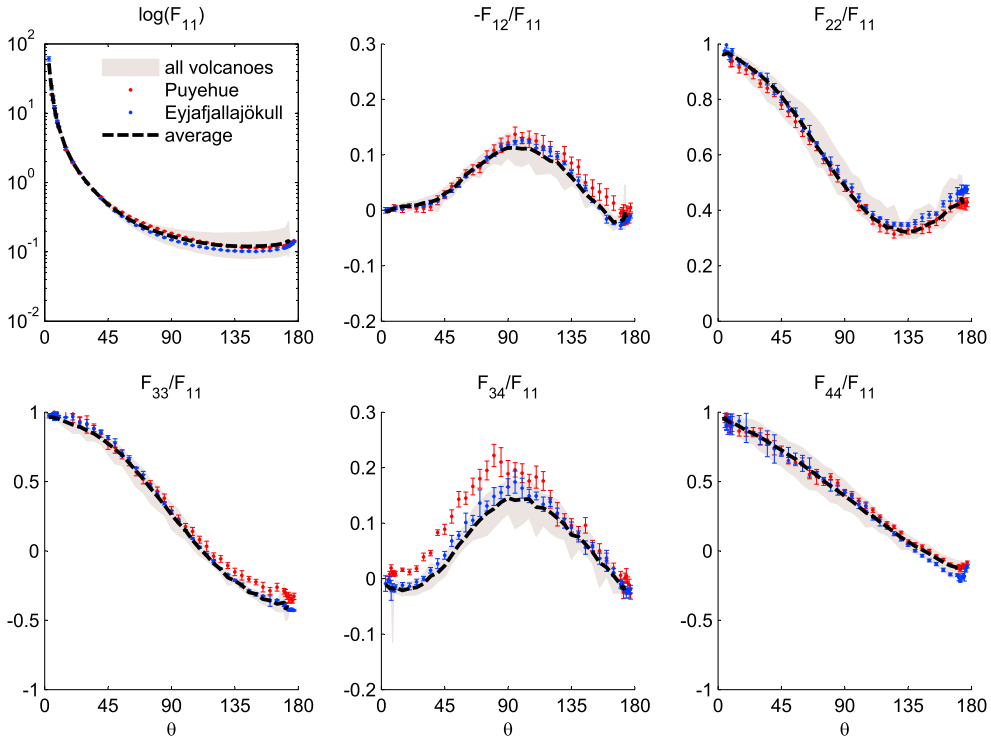

Figure 4. Measured scattering matrices for Puyehue (red) and Eyjafjallajökull (blue) samples for each of the scattering matrix elements. The average scattering matrix of all the volcanic ash particles in the Amsterdam–Granada database and the domain of the span of these particles are also shown.

scattering matrices of nine volcanic ash samples from the Mount St. Helens, Redoubt, Mount Spurr, Lokon, and Pinatubo volcanoes [*Muñoz et al.*, 2004]. Measurements of those nine samples were performed at 632.8 nm. The domains occupied by the measurements used to obtain the average are shown as a gray area in the background of Figure 4. As shown, the measured scattering matrix for the Eyjafjallajökull and Puyehue samples agree well with both the overall features present in the average scattering matrix and their magnitude. It is interesting to note that the F_{34}/F_{11} ratio in the forward scattering lobe for the Puyehue sample has values larger than any other volcano sample measured.

For the use of the results in radiative transfer calculations the full scattering matrix, from 0° to 180°, is needed. Hence, the measured scattering matrix data need to be extended to include the extreme forward and back-scattering angles. This is achieved by constructing so-called synthetic scattering matrices from the measurements in the way described in *Muñoz et al.* [2007] but including conditions at exact forward and backward directions as suggested by *Hovenier and Guirado* [2014].

Tables with the experimental data and the corresponding extrapolated matrices for all samples are available at the Amsterdam-Granada light scattering database http://www.iaa.es/scattering/ [*Muñoz et al.*, 2012].

3. Modeling Approach

To investigate whether ellipsoidal model particles can be used in scattering computations to mimic the optical properties of volcanic ash particles, model simulations based on ellipsoids are compared with laboratory-measured scattering matrices for real volcanic ash samples. Different assumptions about the porosity are tested in the simulations and size distributions of volcanic samples derived using Lorenz-Mie and Frauhofer-based theories are both considered. Apart from the new measurements (performed at a wavelength of 647 nm) and the volcanic ashes average (632.8 nm), measurements at 441.6 nm are also considered for those samples for which the measurements are available, namely, Lokon and Pinatubo.

The scattering matrices and scattering cross sections of the ellipsoids are retrieved from the database of *Meng et al.* [2010], where they are tabulated for various refractive indices (real part Re(m) ranging from 1.1 to 2.1 and imaginary part Im(m) from 0.0005 up to 0.5) and for axis ratios (a_x/a_z and a_y/a_z ranging from unity up to 3.3).

The optical properties for each ellipsoidal shape are obtained from this database using volume-equivalent sizes and then integrated over the measured size distributions (section 2.2) of the volcanic ash samples, after which a Monte Carlo fitting procedure is applied to derive an optimal ellipsoidal shape distribution that minimizes the difference between the modeled and measured scattering matrices.

For computational reasons we need to constrain the fitting of shape distribution into a manageable amount of shapes. We have thus chosen a carefully selected subset of shapes present in the database. Namely, ellipsoids with shapes close to a sphere (values of axis ratios a_x/a_z and a_y/a_z close to unity), but not the sphere itself ($a_x = a_x = a_x$), have been left out of the analysis. This choice is based on previous studies which showed that best-fit shape distributions for mineral dusts consist mostly of noticeably nonspherical shapes [*Merikallio et al.*, 2011, 2013].

For validation, the model results were compared to the experimental data (section 2), and the best-fit was selected based on the cost function E defined as

$$E = \sum_{\theta} \frac{\varrho_\theta [S(\theta) - O(\theta)]^2}{\pi \sigma_\theta^2}, \tag{1}$$

where $S(\theta)$ is the simulated quantity, $O(\theta)$ the corresponding observed quantity, σ_θ the measured scattering angle dependent standard deviation, and ϱ_θ the width of the angular bin. $S(\theta) = P_{xy}(\theta)/P_{11}(\theta)$ and $O(\theta) = F_{xy}(\theta)/F_{11}(\theta)$, where the xy subscript denotes the corresponding scattering matrix element, being 12, 22, 33, 34, or 44. Measurements of the scattering matrix elements include an unknown normalization constant, which can be omitted when only quantities related to the phase function F_{11} are examined. As the phase function itself is not a relative quantity, its cost function is defined slightly differently to make it a relative quantity and thus comparable with the other scattering matrix elements: $E_{11} = \sum_\theta \varrho_\theta/\pi(P_{11}/F_{11} - 1)^2/\sigma_\theta^2$. Note also that this definition automatically assures that the forward angles with much higher absolute values do not dominate the cost function. Each shape-distribution fitting was carried out using multiple initial conditions to better assure that the global best fit is found.

We also made an effort to account for the porosity by applying the effective medium approximation to compute the corresponding effective refractive indices for different degrees of porosity, namely, $m = 1.4 + 0.000758i$ corresponding to a porosity of 31.6%, $1.5 + 0.000921i$ corresponding to 10.9%, and $1.55 + 0.001i$ corresponding to 0% (solid matter) [*Mishchenko et al.*, 2000]. For simplicity, the same values were used for all samples, although in reality they are estimated to have differing refractive indices (see Table 1). This simplification is justifiable by the fact that the estimation of the refractive index has a high uncertainty and is often based on simplifying assumptions of the composition equaling some other well-known substance which may or may not accurately describe the bulk matter composition of the scattering target particle [*Mackie et al.*, 2014]. All the samples were fitted using all assumptions about porosity (different refractive indices). For all our samples, the cost function was best minimized when using the assumed refractive index of the bulk matter, $1.55 + 0.001i$. This implies that either the particles are not porous or, more likely, their porosity does not manifest itself in scattering in such a way that it can be accounted for by using an effective refractive index. The latter is also consistent with findings by [*Nousiainen et al.*, 2011]. However, it was also noted that for some of the samples, in particularly for Eyjafjallajökull, the fits would have slightly improved by using an even smaller imaginary part of the refractive index. For simplicity, we decided to use the bulk matter refractive index for all samples throughout this study.

4. Results

In our calculations we used the size distributions retrieved using both the Fraunhofer and Lorenz-Mie theories. As the size distributions calculated with the Lorenz-Mie theory turned out to provide the best fits, we chose to use those for modeling the scattering matrices for which we had them reliably available for, namely, Eyjafjallajökull, Puyehue, and St. Helens. However, as explained in section 2.2, the Lorenz-Mie theory-based size distributions are not available for Pinatubo, Lokon, Redoubt, and Mt. Spurr ash samples. The original Fraunhofer size distribution was used for these cases.

4.1. Overall Performance of Ellipsoids

In Figure 5 the whole-matrix best-fit ellipsoidal model results based on $m = 1.55 + 0.001i$ are shown for Eyjafjallajökull, Puyehue, and St. Helens volcanic ash samples, for which we had reliable Lorenz-Mie-based

size measurements available. For brevity, only the most commonly used matrix elements (P_{11}, P_{12}/P_{11}, and P_{22}/P_{11}) are shown, although the fitting was performed by optimizing the agreement with all six non-zero matrix elements with equal weights. The phase function P_{11} is shown on a logarithmic scale and normalized such that the integral over the scattering angle θ is

$$\frac{1}{2}\int_0^{\pi} P_{11}(\theta)\sin(\theta)d\theta = 1. \quad (2)$$

The full angle span of the phase function needed to perform this integral has been achieved by extrapolating the measurements with the mean of the model ellipsoid phase functions. Note that here, due to the availability of ellipsoid simulations, we have used this slightly different extrapolation method to that of the released measurements in the Granada database (see section 2.3).

Similar data for the other four volcanic ash samples, with size distributions determined using Fraunhofer theory, are shown in Figure 6. In addition to the measured values, these plots show the results for the best-fit ellipsoids, Lorenz-Mie model (spherical particles), and the equiprobable ellipsoidal distribution, where all shapes are present in equal proportions. Additionally, the whole value span covered by different ellipsoidal shapes is shown as the gray shaded area. It is evident that ellipsoids improve greatly on the performance of spheres in reproducing the optical properties of real ash particles. Still, even the best-fit results are far from perfect and lack performance especially for the depolarization element P_{22}/P_{11}. In part, this may be due to ellipsoids not having rough surfaces, which is not taken into account here [*Nousiainen and Muinonen*, 2007; *Baum et al.*, 2010]. It is noted that the fit from P_{22}/P_{11} could be improved by fitting solely that matrix element, at the expense of other matrix elements for which the fits would then become worse. Overall, ellipsoids perform significantly better than spheres, which are strikingly bad especially with P_{12}/P_{11}, for which they even seem to have the wrong sign, and with P_{22}/P_{11} for which their solution is, by definition, exactly one at all scattering angles.

The last row of plots in Figure 5 shows the best-fit shape distributions of ellipsoids for Eyjafjallajökull, St. Helens, and Puyehue, respectively, as a function of the model particle shape axis ratios, a_x/a_z and a_y/a_z. In this projection the prolate spheroids ($a_x > a_y = a_z$) fall on the x axis, and the oblate spheroids ($a_y = a_x > a_z$) are on the diagonal. The particle nonsphericity increases toward the right and up. It can be seen that the best-fit shape distributions differ quite significantly case by case but nevertheless share some common characteristics: they all seem to have distributions weighted on the prolate side but curiously include only a few pure prolates (the x axis). The same trend can be seen in Figure 7a, where the average shape distribution of all seven samples at all wavelengths is shown. It can be seen that the average best-fit distributions, when fitting the whole matrix, consists mostly of pure ellipsoids and slightly deformed spheroids. The pattern is delightfully similar for the shorter and longer wavelengths, when considered separately (Figures 7b and 7c).

4.2. Validation in the AATSR Instrument Framework

Satellites are important in observing volcanic ash clouds, since they can provide a daily view of an extended area of hundreds to thousands of square kilometers, depending on the instrument characteristics. The purpose of this section is to perform an initial assessment of our results in the context of satellite retrievals. For this, we use the AATSR as an example because this instrument has been used by our group previously, including prior volcanic ash studies by *Virtanen et al.* [2014].

AATSR flew onboard ENVISAT (ENVIronmental SATelite, operating 2002–2012). It offers seven wavebands in the visible (VIS), near-infrared (NIR), and thermal infrared (TIR) [*Llewellyn-Jones et al.*, 2001] and is used for remote sensing of aerosol properties [*de Leeuw et al.*, 2013], as well as for measuring volcanic ash plume properties [*Grainger et al.*, 2013; *Virtanen et al.*, 2014]. AATSR has the advantage of providing measurements at two viewing angles (near-nadir and 55° forward), and the observations in the NIR and TIR wavebands facilitate the discrimination between volcanic ash and water or ice clouds. Importantly, the AATSR, similar to most other satellite instruments, measures only the intensity of radiation (of which the angle distribution is described by $P_{11}(\theta)$) [*Tanré et al.*, 2011]. Some satellite based instruments, however, e.g., POLDER (POLarization and Directionality of the Earth's Reflectances) aboard PARASOL, can also measure the linear polarization of the radiation (P_{12}/P_{11}) [*Deschamps et al.*, 1994]. POLDER has recently also been used to investigate airborne volcanic ash from Eyjafjallajökull [*Waquet et al.*, 2014].

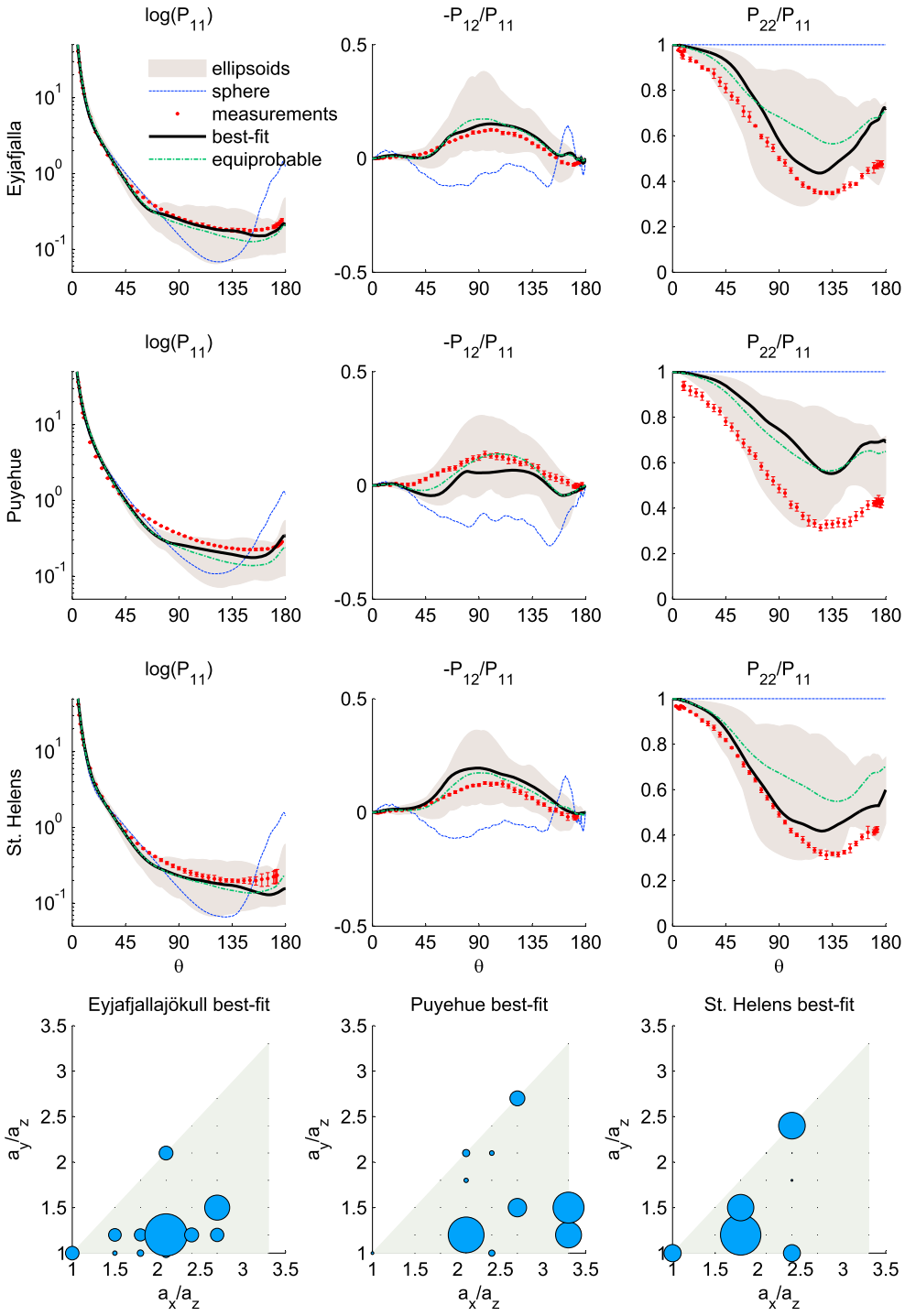

Figure 5. Best-fit ellipsoid model results and shape distributions (blue balls) for volcanic ash from Eyjafjallajökull, Puyehue, and Helens (top to bottom, and from left to right in the last row of plots). Best-fit model results are shown for matrix elements P_{11} (shown on a logarithmic scale), P_{12}/P_{11}, and P_{22}/P_{11}. The bottom row of plots shows the best-fit shape distributions for each of these ash types: along the axis are plotted the relative aspect ratios of the two biggest axes of the ellipsoid model particles, when the smallest axis is of unity length. The marker sizes are corresponding to the relative weighs of corresponding shapes, and the gray shading indicates the area covered by ellipsoids (sphere is excluded).

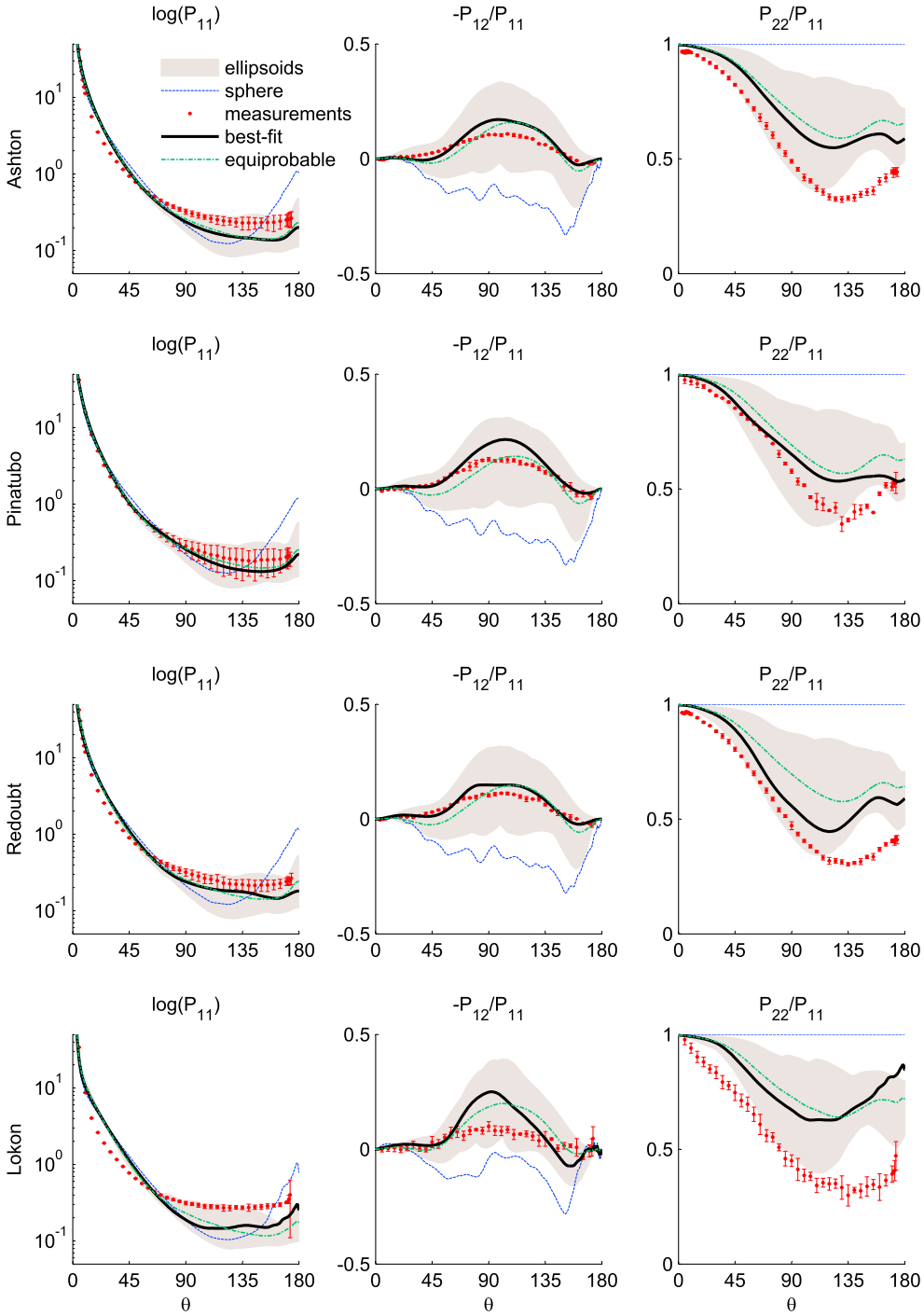

Figure 6. First three scattering matrix elements (columns) and best-fit ellipsoid models for four volcanic ash samples (rows): the best-fit model results for matrix elements P_{11} (shown on a logarithmic scale), P_{12}/P_{11}, and P_{22}/P_{11} for the Ashton, Pinatubo, Redoubt, and Lokon volcanic ashes are shown.

Depending on the across track position, the viewing angle of AATSR varies between 0° and 22° for the near-nadir view and between 52° and 56° for the forward view. Taking into account the Sun-satellite geometry, the scattering angle for AATSR measurements varies mostly between 50° and 170°. We will thus consider how our results are affected, when we account for the fact that AATSR measurements do not cover the whole angular span from exact backscattering to forward scattering.

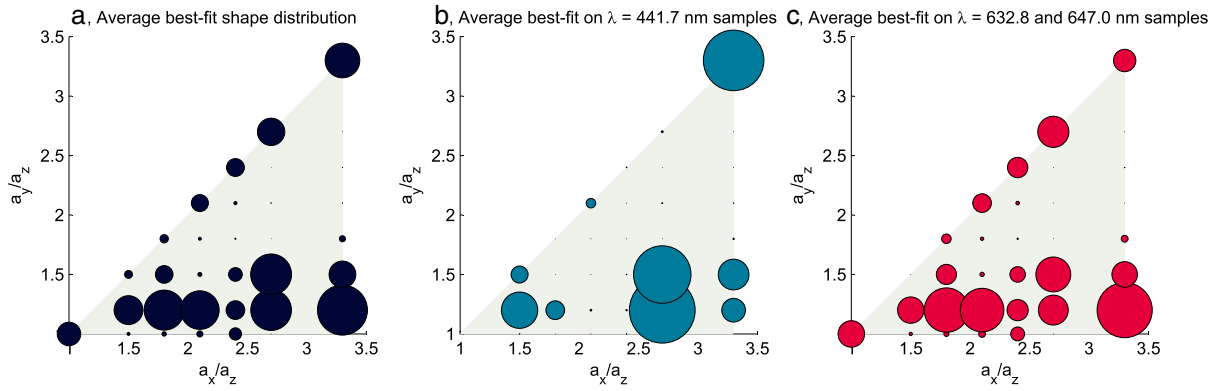

Figure 7. Best-fit shape distributions shown averaged (left) over all samples and wavelengths, (center) for the shorter wavelength, and (right) for the longer wavelength. Axes on the graph denote the major axis ratios of the model particles. The shaded area in the background denotes the region spanned by the model ellipsoids considered in this study.

Multiple scattering becomes substantial with large aerosol optical depths, in which case the signal measured by the AATSR will be affected significantly also by polarization components and all scattering angles are relevant. It has been shown, for example, that neglecting polarization may then lead to considerable errors [*Moreno et al.*, 2002; *Stam and Hovenier*, 2005]. It can thus be expected that the ellipsoids may provide substantial improvements on simpler model particles (spheres or spheroids [*Dubovik et al.*, 2006; *Yang et al.*, 2007]) as their performance in reproducing the whole scattering matrix is better [*Bi et al.*, 2009]. Thus, for this case, the investigation carried out in the previous section is appropriate, but the assessment of the performance requires full radiative transfer simulations and is outside the scope of the present study. We will consider these and full retrieval tests in a follow-up study.

When the aerosol optical depth is low, however, which is usually the situation [*Remer et al.*, 2008; *Colarco et al.*, 2014], single scattering dominates the aerosol signal measured by AATSR. For testing the performance of ellipsoids in this situation, only the phase function is required. The approach is then, as a sensitivity test, to repeat the treatment of section 3, but only considering the relevant angular range and scattering-matrix elements. However, for curiosity, we will also consider fitting simultaneously both P_{11} and P_{12}/P_{11} matrix elements, as this would be relevant for the POLDER instrument.

The best-fit shape distributions for the AATSR case, when fitting only the phase function P_{11} or both phase function and depolarization P_{12}/P_{11} simultaneously, are shown in Figures 8 and 9, respectively. The fits themselves (not shown) were, as can be expected, better than in the cases where the whole matrix was fitted simultaneously (Figures 5 and 6). Improvement over the spheres was evident. Here again, as previously for the whole matrix in Figure 7, we can see the tendency of best-fits to avoid pure prolate shapes. Also, the phase function fit especially seems to have only moderately asymmetric shapes involved with axis ratios smaller than 2.5. Fits for the different wavelengths appear similar, which is encouraging. Also, as expected, when we only

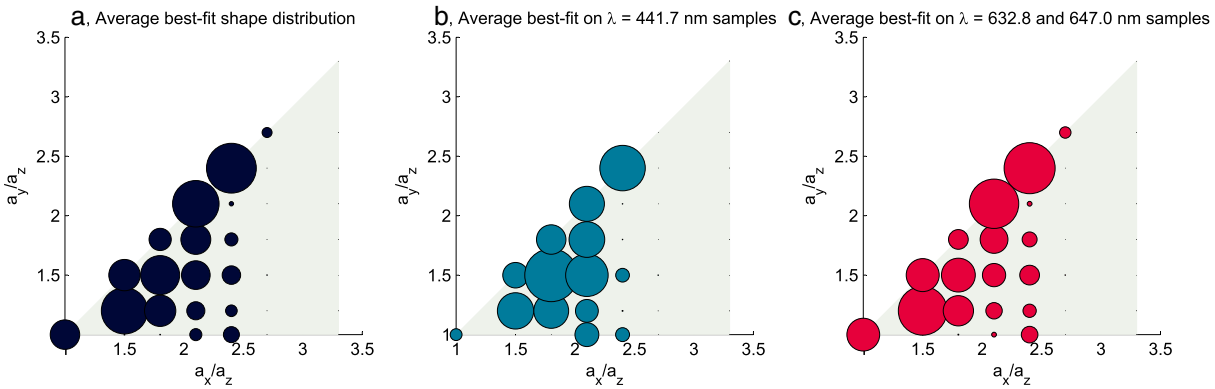

Figure 8. Best-fit shape distributions, when only the P_{11} element of the scattering matrix is fitted and only for the AATSR angle span. Labeling on this figure is the same as in Figure 7.

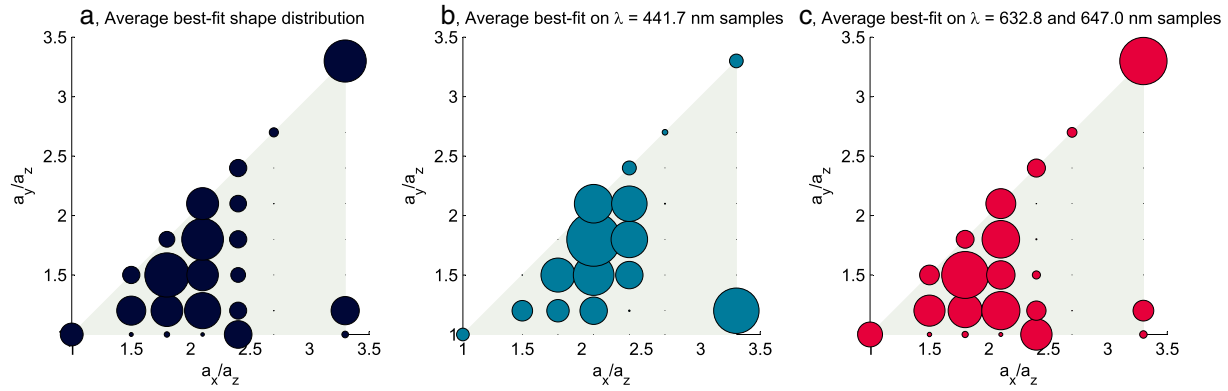

Figure 9. Best-fit shape distributions, when both the P_{11} and P_{12} elements of the scattering matrix are fitted and only for the AATSR angle span. Labeling on this figure is the same as in Figure 7.

focus on a certain angle range, the fitting improves in that angle range but loses precision at other angles. The same inevitably happens when the fitting is concentrated on just some matrix elements and the others are omitted, i.e., the fits for the other matrix elements considerably worsen, while those that are considered are fitted quite well.

4.3. Suggested Generic Shape Distribution

The good performance, and the similarity of the best-fit distributions to those obtained in section 4.2 suggest that ellipsoids will improve the performance of the AATSR retrieval. An equiprobable shape distribution, although omitting some of the special features of the best-fit distributions, provides an adequately working first guess alternative for the best-fit shape distribution. Moreover, for the AATSR satellite measurements point of view, as can be deduced from Figure 8, a more refined and yet symmetric shape distribution could be formed by an equiprobable distribution from which all the model particles with axis ratios larger than 2.5 would be discarded. Even further refinement could be achieved by omitting pure prolate shapes.

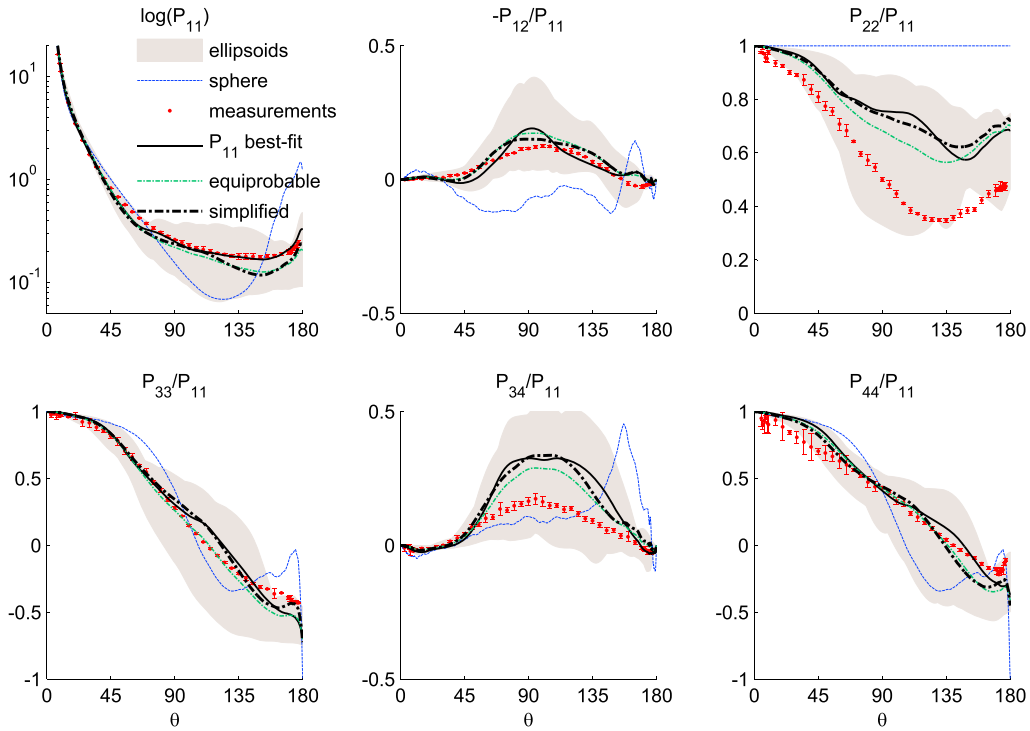

Figure 10. Whole scattering matrix of Eyjafjallajökull: measurements and models with different shape distributions are shown. The best-fit model is fitted solely for P_{11}.

This kind of more refined shape distribution and an equiprobable distribution are compared for Eyjafjallajökull in Figure 10, where the whole scattering matrix is shown when the fits are performed only for the P_{11} element. It can be seen how the best-fit shape distribution (solid black line) follows the measurements (red marks) for the P_{11} element quite well but performs equally badly, as expected, or even worse for the other elements than the equiprobable distribution (green line). The suggested refined shape distribution (shown as the dashed black line) does not markedly improve on the equiprobable distribution in modeling the phase function and performs visibly worse on fitting the measurements for elements P_{22}/P_{11} and P_{34}/P_{11}. The performance of the refined shape distribution for the other samples was similar to that from Eyjafjallajökull. Thus we conclude that the more refined shape distribution considered here is not worth the added effort and the simpler equiprobable distribution is the most reasonable first-guess distribution which can be expected to improve significantly on Mie models.

5. Summary and Conclusions

We present new measurements of the scattering matrices as functions of the scattering angle of two volcanic ash samples corresponding to the Eyjafjallajökull and Puyehue volcanic eruptions. The samples were collected after the April 2010 and June 2011 eruptions, respectively. Measurements are performed at 647 nm covering the scattering angle range from 3° to 177°. To facilitate the use of the experimental scattering matrices for multiple-scattering calculations, we have obtained synthetic scattering matrices based on the measurements in the full scattering angle range from 0° to 180°. Tables of the measured and synthetic scattering matrices are available in the Amsterdam-Granada Light Scattering Database: www.iaa.es/scattering. The data are freely available on request with citation of this paper and [*Muñoz et al.*, 2012].

We have used ellipsoidal shapes in an effort to produce scattering matrix elements measured from samples collected near various volcanic sources. This was done in order to assess whether ellipsoidal model particles could be used to model single scattering of light by volcanic ash particles. Note that the retrieved shape distributions do not necessarily reflect the real sample particle shape distributions. For example, it has been shown for spheroids that the best-fit shape distribution of model shapes do not clearly correlate with the target shape distribution [*Nousiainen et al.*, 2011].

The best-fitting shape distributions of ellipsoidal model particles were sought and their fits to the measurements assessed both for the whole scattering matrix and from the point of view of observations available from the AATSR instrument (only phase function at a certain angle span), as well as from the point of view of satellite instruments able to also measure the polarization (combination of phase function and linear polarization element of the scattering matrix, P_{12}/P_{11}) separately. The results could be used for example to improve data interpretation from remote sensing satellites such as AATSR.

Ellipsoids prove to be rather good shapes for modeling the optical properties of volcanic ash for all the samples and at all the wavelengths tested here. Although considerably improving over spherical model particles, they nevertheless have also shortcomings. The depolarization P_{22}/P_{11} turns out to be especially hard to fit adequately. The results imply that ellipsoids, conveniently available in a well-organized database by *Meng et al.* [2010], provide an adequately working set of model shapes for forward modeling applications. For inverse problems, their use may be more problematic. For example, it was shown by (O. Kemppinen et al., submitted manuscript, 2015) that ellipsoids do not seem be suitable for retrievals of refractive index, and the same probably holds true for retrievals of other physical characteristics as well. This might also explain why we obtained better results when using the higher refractive index, representative of the bulk matter ($m = 1.55 + 0.001i$), than with the estimated smaller refractive indices of the more porous particles, although these smaller indices would have been closer to the estimated refractive indices of the ash samples (Table 1). Regardless of these issues, however, the ellipsoids are the best currently available model particles for real applications due their considerable parameter space to consider. In particular, the required range of size parameters involved is substantial, demanding further development and ever improving computing power for more sophisticated modelling approaches.

Finally, for forward modeling the equiprobable shape distribution of ellipsoids was found to be a very good compromise between simplicity and performance. A more refined generalized shape distribution was also tested and discussed, but the advantage it provided over more general equiprobable distribution was small at best. The equiprobable shape distribution is thus recommended as a first-guess shape distribution for applications where the shape distributions cannot be optimized for the purpose.

Acknowledgments
We thank Zhaokai Meng for letting us use his ellipsoid database, without which this study would not have materialized in its current form. It is a pleasure also to thank Evgenia Ilinskaya and Alberto Caselli for providing the Eyjafjallajökull and Puyehue samples, respectively. The SEM pictures were taken at the Scientific Instrumentation Center of the University of Granada. We are indebted to Isabel Guerra-Tschuschke for her support with the SEM. This work was supported by the Plan Nacional de Astronomia y Astrofisica (contracts AYA2009-08190 and AYA2012-39691), the Junta de Andalucia (contract P09-FMQ-455), the VAST project by ESA (ESA-ESRIN contract 4000105701/12/I-LG), the Finnish Funding Agency for Technology and Innovation (Tekes) (grant 3155/31/2009), the Academy of Finland (grant 255718), the Academy of Finland Centre on Excellence in Atmospheric Science (project 272041), and the Top-level Research Initiative (TRI) CRAICC (Cryosphere-atmosphere interactions in a changing Arctic climate). Volcanic ash particle measurements presented in this paper are freely available at the Amsterdam-Granada Light Scattering Database (www.iaa.es/scattering; *Muñoz et al.* [2012]). Alternatively, data can be requested from Olga Muñoz (olga@iaa.es).

References

Baum, B. A., P. Yang, Y. -X. Hu, and Q. Feng (2010), The impact of ice particle roughness on the scattering phase matrix, *J. Quant. Spectrosc. Radiat. Transfer*, *111*(17–18), 2534–2549, doi:10.1016/j.jqsrt.2010.07.008.

Baxter, P. J., R. S. Bernstein, H. Falk, J. French, and R. Ing (1982), Medical aspects of volcanic disasters: An outline of the hazards and emergency response measures, *Disasters*, *6*(4), 268–276, doi:10.1111/j.1467-7717.1982.tb00549.x.

Bertrand, C., J.-P. van Ypersele, and A. Berger (1999), Volcanic and solar impacts on climate since 1700, *Clim. Dyn.*, *15*(5), 355–367, doi:10.1007/s003820050287.

Bertrand, C., J.-P. van Ypersele, and A. Berger (2002), Are natural climate forcings able to counteract the projected anthropogenic global warming?, *Clim. Change*, *55*(4), 413–427, doi:10.1023/A:1020736804608.

Bi, L., P. Yang, G. Kattawar, and R. Kahn (2009), Single-scattering properties of triaxial ellipsoidal particles for a size parameter range from the rayleigh to geometric-optics regimes, *Appl. Opt.*, *48*(1), 114–126, doi:10.1016/j.jaerosci.2010.02.008.

Bignami, C., V. Bosi, L. Costantin, C. Cristiani, F. Lavigne, and P. Thierry (Eds.) (2013), *Handbook for Volcanic Risk Management — Prevention, Crisis Management, Resilience*, MIAVITA, Orleans, France.

Casadevall, T. J. (1994), The 1989–1990 eruption of Redoubt volcano, Alaska: Impacts on aircraft operations, *J. Volcanol. Geotherm. Res.*, *62*(1–4), 301–316, doi:10.1016/0377-0273(94)90038-8.

Colarco, P. R., R. A. Kahn, L. A. Remer, and R. C. Levy (2014), Impact of satellite viewing-swath width on global and regional aerosol optical thickness statistics and trends, *Atmos. Meas. Tech.*, *7*(7), 2313–2335, doi:10.5194/amt-7-2313-2014.

de Leeuw, G., et al. (2013), Evaluation of seven European aerosol optical depth retrieval algorithms for climate analysis, *Remote Sensing of Environment*, doi:10.1016/j.rse.2013.04.023, in press.

Deschamps, P., F. M. Bréon, M. Leroy, A. Podaire, A. Bricaud, J. Buriez, and G. Seze (1994), The POLDER mission: Instrument characteristics and scientific objectives, *IEEE Trans. Geosci. Remote Sens.*, *32*, 598–615, doi:10.1109/36.297978.

Dubovik, O., et al. (2006), Application of spheroid models to account for aerosol particle nonsphericity in remote sensing of desert dust, *J. Geophys. Res.*, *111*, D11208, doi:10.1029/2005JD006619.

Grainger, R., D. Peters, G. Thomas, A. Smith, R. Siddans, E. Carboni, and A. Dubhia (2013), Measuring volcanic plume and ash properties from space, *Geol. Soc. London Spec. Publ.*, *380*(1), 293–320, doi:10.1144/SP380.7.

Gudmundsson, G. (2011), Respiratory health effects of volcanic ash with special reference to Iceland. A review, *Clin. Respir. J.*, *5*(1), 2–9, doi:10.1111/j.1752-699X.2010.00231.x.

Gudmundsson, M., G. Larsen, A. Höskuldsson, and A. Gylfason (2008), Volcanic hazards in Iceland, *Jökull*, *58*, 251–268.

Guffanti, M., D. J. Schneider, K. L. Wallace, T. Hall, D. R. Bensimon, and L. J. Salinas (2010), Aviation response to a widely dispersed volcanic ash and gas cloud from the August 2008 eruption of Kasatochi, Alaska, USA, *J. Geophys. Res.*, *115*, D00L19, doi:10.1029/2010JD013868.

Hansen, J. E., and L. D. Travis (1974), Light scattering in planetary atmospheres, *Space Sci. Rev.*, *16*, 527–610, doi:10.1007/BF00168069.

Heiken, G. (1974), *An Atlas of Volcanic Ash*, Smithsonian Institution Press, Washington, D. C.

Horwell, C., and P. Baxter (2006), The respiratory health hazards of volcanic ash: A review for volcanic risk mitigation, *Bull. Volcanol.*, *69*(1), 1–24, doi:10.1007/s00445-006-0052-y.

Hovenier, J. (2000), Measuring scattering matrices of small particles at optical wavelengths, in *Light Scattering by Nonspherical Particles*, edited by M. I. Mishchenko, J. W. Hovenier, and L. D. Travis, pp. 147–172, Academic Press, San Diego.

Hovenier, J., and D. Guirado (2014), Zero slopes of the scattering function and scattering matrix for strict forward and backward scattering by mirror symmetric collections of randomly oriented particles, *J. Quant. Spectrosc. Radiat. Transfer*, *133*, 596–602, doi:10.1016/j.jqsrt.2013.09.023.

Hovenier, J., H. C. van de Hulst, and C. V. M. van der Meer (1986), Conditions for the elements of the scattering matrix, *Astron. Astrophys.*, *157*, 301–310.

Hyde, W. T., and T. J. Crowley (2000), Probability of future climatically significant volcanic eruptions, *J. Clim.*, *13*, 1445–1450, doi:10.1175/1520-0442(2000)013<1445:LOFCSV>2.0.CO;2.

Kahn, R. A., and J. Limbacher (2012), Eyjafjallajökull volcano plume particle-type characterization from space-based multi-angle imaging, *Atmos. Chem. Phys.*, *12*(20), 9459–9477, doi:10.5194/acp-12-9459-2012.

Kahnert, M., T. Nousiainen, and H. Lindqvist (2014), Review: Model particles in atmospheric optics, *J. Quant. Spectrosc. Radiat. Transfer*, *146*, 41–58.

Konert, M., and J. Vandenberghe (1997), Comparison of laser grain size analysis with pipette and sieve analysis: A solution for the underestimation of the clay fraction, *Sedimentology*, *44*(3), 523–535, doi:10.1046/j.1365-3091.1997.d01-38.x.

Kylling, A., M. Kahnert, H. Lindqvist, and T. Nousiainen (2014), Volcanic ash infrared signature: Porous non-spherical ash particle shapes compared to homogeneous spherical ash particles, *Atmos. Meas. Tech.*, *7*(4), 919–929, doi:10.5194/amt-7-919-2014.

Llewellyn-Jones, D., M. C. Edwards, C. T. Mutlow, A. R. Birks, I. J. Barton, and H. Tait (2001), AATSR: Global-change and surface-temperature measurements from Envisat, *ESA Bull.*, *105*, 11–21.

Mackie, S., S. Millington, and I. M. Watson (2014), How assumed composition affects the interpretation of satellite observations of volcanic ash, *Meteorol. Appl.*, *21*(1), 20–29, doi:10.1002/met.1445.

Maria, A., and S. Carey (2002), Using fractal analysis to quantitatively characterize the shapes of volcanic particles, *J. Geophys. Res.*, *107*(B11), 2283, doi:10.1029/2001JB000822.

Mather, T., D. Pyle, and C. Oppenheimer (2013), *Tropospheric Volcanic Aerosol*, pp. 189–212, AGU, Washington, D. C., doi:10.1029/139GM12.

McGee, T. J., P. Newman, M. Gross, U. Singh, S. Godin, A. -M. Lacoste, and G. Megie (1994), Correlation of ozone loss with the presence of volcanic aerosols, *Geophys. Res. Lett.*, *21*(25), 2801–2804, doi:10.1029/94GL02350.

Meng, Z., P. Yang, G. Kattawar, L. Bi, K. Liou, and I. Laszlo (2010), Single-scattering properties of tri-axial ellipsoidal mineral dust aerosols: A database for application to radiative transfer calculations, *J. Aerosol Sci.*, *41*, 501–512, doi:10.1016/j.jaerosci.2010.02.008.

Merikallio, S., H. Lindqvist, T. Nousiainen, and M. Kahnert (2011), Modelling light scattering by mineral dust using spheroids: Assessment of applicability, *Atmos. Chem. Phys.*, *11*(11), 5347–5363, doi:10.5194/acp-11-5347-2011.

Merikallio, S., T. Nousiainen, M. Kahnert, and A. -M. Harri (2013), Light scattering by the Martian dust analog, palagonite, modeled with ellipsoids, *Opt. Express*, *21*, 17,972–17,985, doi:10.1364/OE.21.017972.

Mishchenko, M. I., J. W. Hovenier, and L. D. Travis (Eds.) (2000), *Light Scattering by Nonspherical Particles*, 690 pp., Academic Press, San Diego, Calif.

Moreno, F., O. Muñoz, J. López-Moreno, A. Molina, and J. Ortiz (2002), A Monte Carlo code to compute energy fluxes in cometary nuclei, *Icarus*, *156*(2), 474–484, doi:10.1006/icar.2001.6806.

Muñoz, O., H. Volten, J. W. Hovenier, B. Veihelmann, W. J. van der Zande, L. B. F. M. Waters, and W. I. Rose (2004), Scattering matrices of volcanic ash particles of Mount St. Helens, Redoubt, and Mount Spurr volcanoes, *J. Geophys. Res.*, *109*, D16201, doi:10.1029/2004JD004684.

Muñoz, O., H. Volten, J. W. Hovenier, T. Nousiainen, K. Muinonen, D. Guirado, F. Moreno, and L. B. F. M. Waters (2007), Scattering matrix of large Saharan dust particles: Experiments and computations, *J. Geophys. Res.*, *112*, D13215, doi:10.1029/2006JD008074.

Muñoz, O., F. Moreno, D. Guirado, J. Ramos, A. López, F. Girela, J. Jerónimo, L. Costillo, and I. Bustamante (2010), Experimental determination of scattering matrices of dust particles at visible wavelengths: The IAA light scattering apparatus, *J. Quant. Spectrosc. Radiat. Transfer*, *111*(1), 187–196, doi:10.1016/j.jqsrt.2009.06.011.

Muñoz, O., F. Moreno, D. Guirado, J. Ramos, H. Volten, and J. Hovenier (2011), The IAA cosmic dust laboratory: Experimental scattering matrices of clay particles, *Icarus*, *211*(1), 894–900, doi:10.1016/j.icarus.2010.10.027.

Muñoz, O., F. Moreno, D. Guirado, D. Dabrowska, H. Volten, and J. Hovenier (2012), The Amsterdam–Granada light scattering database, *J. Quant. Spectrosc. Radiat. Transfer*, *113*(7), 565–574, doi:10.1016/j.jqsrt.2012.01.014.

Newman, S. M., L. Clarisse, D. Hurtmans, F. Marenco, B. Johnson, K. Turnbull, S. Havemann, A. J. Baran, D. O'Sullivan, and J. Haywood (2012), A case study of observations of volcanic ash from the Eyjafjallajökull eruption: 2. Airborne and satellite radiative measurements, *J. Geophys. Res.*, *117*, D00U13, doi:10.1029/2011JD016780.

Nousiainen, T., and K. Muinonen (2007), Surface-roughness effects on single-scattering properties of wavelength-scale particles, *J. Quant. Spectrosc. Radiat. Transfer*, *106*, 389–397, doi:10.1016/j.jqsrt.2007.01.024.

Nousiainen, T., M. Kahnert, and H. Lindqvist (2011), Can particle shape information be retrieved from light-scattering observations using spheroidal model particles?, *J. Quant. Spectrosc. Radiat. Transfer*, *112*(13), 2213–2225, doi:10.1016/j.jqsrt.2011.05.008.

Pollack, J., O. Toon, and B. Khare (1974), Optical properties of some terrestrial rocks and glasses, *Icarus*, *19*, 372–389, doi:10.1016/0019-1035(73)90115-2.

Prata, A. J., C. Zehner, and K. Stebel (2014), Earth observations and volcanic ash, A report of the ESA/Eumesat Workshop, 4–7 March, 2013, doi:10.5270/atmva-14-04.

Remer, L. A., et al. (2008), Global aerosol climatology from the modis satellite sensors, *J. Geophys. Res.*, *113*, D14S07, doi:10.1029/2007JD009661.

Riley, C. M., W. I. Rose, and G. J. S. Bluth (2003), Quantitative shape measurements of distal volcanic ash, *J. Geophys. Res.*, *108*(B10), 2504, doi:10.1029/2001JB000818.

Rocha-Lima, A., J. V. Martins, L. A. Remer, N. A. Krotkov, M. H. Tabacniks, Y. Ben-Ami, and P. Artaxo (2014), Optical, microphysical and compositional properties of the Eyjafjallajökull volcanic ash, *Atmos. Chem. Phys. Discuss.*, *14*(9), 13,271–13,300, doi:10.5194/acpd-14-13271-2014.

Schumann, U., et al. (2011), Airborne observations of the Eyjafjalla volcano ash cloud over Europe during air space closure in April and May 2010, *Atmos. Chem. Phys.*, *11*(5), 2245–2279, doi:10.5194/acp-11-2245-2011.

Sparks, R. (2003), Forecasting volcanic eruptions, *Earth Planet. Sci. Lett.*, *210*(1–2), 1–15, doi:10.1016/S0012-821X(03)00124-9.

Stam, D. M., and J. W. Hovenier (2005), Errors in calculated planetary phase functions and albedos due to neglecting polarization, *Astron. Astrophys.*, *444*(1), 275–286, doi:10.1051/0004-6361:20053698.

Stevenson, J. A., S. C. Millington, F. M. Beckett, G. T. Swindles, and T. Thordarson (2015), Big grains go far: Reconciling tephrochronology with atmospheric measurements of volcanic ash, *Atmos. Meas. Tech. Discuss.*, *8*(1), 65–120, doi:10.5194/amtd-8-65-2015.

Tanré, D., F. M. Bréon, J. L. Deuzé, O. Dubovik, F. Ducos, P. François, P. Goloub, M. Herman, A. Lifermann, and F. Waquet (2011), Remote sensing of aerosols by using polarized, directional and spectral measurements within the A-train: The PARASOL mission, *Atmos. Meas. Tech.*, *4*(7), 1383–1395, doi:10.5194/amt-4-1383-2011.

Virtanen, T. H., P. Kolmonen, E. Rodríguez, L. Sogacheva, A. -M. Sundström, and G. de Leeuw (2014), Ash plume top height estimation using AATSR, *Atmos. Meas. Tech.*, *7*(8), 2437–2456, doi:10.5194/amt-7-2437-2014.

Volten, H., O. Muñoz, J. F. de Haan, W. Vassen, J. W. Hovenier, K. Muinonen, and T. Nousiainen (2001), Scattering matrices of mineral aerosol particles at 441.6 nm and 632.8 nm, *J. Geophys. Res.*, *106*(D15), 17,375–17,401, doi:10.1029/2001JD900068.

Waquet, F., F. Peers, P. Goloub, F. Ducos, F. Thieuleux, Y. Derimian, J. Riedi, M. Chami, and D. Tanré (2014), Retrieval of the Eyjafjallajökull volcanic aerosol optical and microphysical properties from POLDER/PARASOL measurements, *Atmos. Chem. Phys.*, *14*(4), 1755–1768, doi:10.5194/acp-14-1755-2014.

Yang, P., Q. Feng, G. Hong, G. W. Kattawar, W. J. Wiscombe, M. I. Mishchenko, O. Dubovik, I. Laszlo, and I. N. Sokolik (2007), Modeling of the scattering and radiative properties of nonspherical dust-like aerosols, *J. Aerosol Sci.*, *38*(10), 995–1014, doi:10.1016/j.jaerosci.2007.07.001.